



JGR Space Physics

RESEARCH ARTICLE

10.1029/2019JA026628

Key Points:

- Comprehensive set of magnetopause and bow shock crossings spanning the entire Cassini mission presented
- Crossings used in conjunction with boundary models to infer upstream solar wind dynamic pressure and range of standoff distances
- Rapid traversals of magnetosheath explored in context of rapidly changing external conditions

Supporting Information:

- Supporting Information S1
- Table S1

Correspondence to:

C. M. Jackman,
c.jackman@soton.ac.uk

Citation:

Jackman, C. M., Thomsen, M. F., & Dougherty, M. K. (2019). Survey of Saturn's magnetopause and bow shock positions over the entire Cassini mission: Boundary statistical properties and exploration of associated upstream conditions. *Journal of Geophysical Research: Space Physics*, 124, 8865–8883. <https://doi.org/10.1029/2019JA026628>

Received 16 FEB 2019

Accepted 12 AUG 2019

Accepted article online 14 OCT 2019

Published online 21 NOV 2019

Survey of Saturn's Magnetopause and Bow Shock Positions Over the Entire Cassini Mission: Boundary Statistical Properties and Exploration of Associated Upstream Conditions

C. M. Jackman¹ , M. F. Thomsen^{2,3} , and M. K. Dougherty⁴

¹Department of Physics and Astronomy, University of Southampton, Southampton, UK, ²Planetary Science Institute, Tucson, AZ, USA, ³Los Alamos National Laboratory, Los Alamos, NM, USA, ⁴Blackett Laboratory, Imperial College London, London, UK

Abstract The Cassini spacecraft orbited the planet Saturn from July 2004 to September 2017, and its varied orbital trajectory took it across the magnetopause and bow shock boundaries multiple times, at varying radial distances, local times, latitudes, and phases of the solar cycle. Here we present a comprehensive list of these boundary crossings, derived primarily using data from the Cassini magnetometer instrument, with cross-validation against the electron spectrometer data where available. There are a multitude of scientific avenues for exploitation of this list. In this work, we examine the variability in boundary location and use the crossing times in concert with models of the bow shock and magnetopause to infer the upstream solar wind dynamic pressure at the times of crossings. This analysis allows us to understand the limitations of the Cassini trajectory for studying boundary physics under a range of solar wind driving conditions. In addition, rapid traversals of the magnetosheath are used to estimate the range of speeds of boundary motion.

1. Introduction

Like other planetary magnetospheres, Saturn's magnetosphere is bounded by a magnetopause, upstream of which lies the magnetosheath and the **bow shock**. Saturn's upstream environment represents a different parameter space to that of the Earth. For example, due to the weaker solar wind at 9 AU, the strong winding of the **interplanetary magnetic field (IMF)** into a Parker spiral-like configuration, and the dominance of **corotating interaction regions (CIRs)** and **merged interaction regions (MIRs)**, the upstream solar wind exhibits a distinctive structure that differs considerably from the solar wind upstream from the Earth (e.g., Jackman et al., 2004; Jackman & Arridge, 2011 and references therein).

The ability of the solar wind at Saturn to influence global magnetospheric dynamics is a topic of some debate. Both the magnetopause and bow shock boundaries are shown to be influenced by factors internal to the magnetosphere, such as planetary period oscillations, which can periodically change the magnetopause position by up to $2 R_S$ ($1 R_S = 60,268$ km; e.g., Clarke et al., 2006, 2010), with other magnetopause motions suggested to be linked to plasmoid release (Zieger et al., 2010) and surface waves (Mistry et al., 2014). **No strong link between magnetopause position and IMF direction has been found** (Jia et al., 2012), implying that erosion due to dayside reconnection may be minimal. The shape of the magnetopause boundary itself is influenced by the magnetodisk pressure inflating the equatorial magnetosphere significantly more than the high-latitude magnetosphere, leading to clear polar flattening (Pilkington et al., 2014). While at Earth simple pressure balance arguments considering upstream solar wind flow against magnetic pressure from the magnetosphere give the approximate location of the magnetopause boundary, at Saturn we must take into account the role of the moon Enceladus, which acts as a significant internal source of plasma. The pressure associated with the suprathermal component of this internally generated plasma acts to inflate the magnetosphere far beyond the size that would be expected from a simple magnetic pressure calculation (Pilkington et al., 2015a). It is thus possible that even under conditions of steady solar wind, the magnetopause boundary may move significantly due to changes in internal plasma content (Jia et al., 2012; Pilkington et al., 2015a).

Between the bow shock and magnetopause lies the magnetosheath, a region of shocked solar wind, which is influenced heavily by the processes that take place within the bow shock, and a region whose properties can influence the interaction across the magnetopause. Thus, the magnetosheath is a critical region, and several authors have sought to explore its statistical properties.

Sergis et al. (2013) selected intervals between 2004 and 2011 when Cassini was moving for more than 24 hr continuously in the magnetosheath and used this database to explore plasma, energetic particle, and magnetic field properties such as number density, temperature, plasma beta, and composition. They focused on the presence of water group (W+) ions detected in the sheath and described the escape of these energetic ions as a function of energy and pitch angle, revealing occasional leakage of heavy energetic ions upstream from the bow shock. Burkholder et al. (2017) surveyed Cassini Plasma Spectrometer (CAPS) ion flow data in the magnetosheath to illustrate significant flow differences prenoon and postnoon, and used the magnetic field data to show rotation of the IMF vector northward from the magnetopause nose toward the flanks. Sulaiman et al. (2017) showed that the impact of polar flattening of the magnetopause is to generate shorter streamline paths over the poles and hence greater pressure gradient, which ultimately twists the field. Importantly, this leads to drastically different conditions at the magnetopause from those predicted based on axisymmetric assumptions. Thomsen et al. (2018) compiled an extensive data set of magnetosheath measurements based on data from CAPS, MAG, and MIMI, extending from 2004 day 299 to 2012 day 151. This data set allowed the exploration of features such as local time dependence of various magnetosheath parameters. They also presented a new method to use magnetosheath properties to estimate the upstream solar wind speed.

With all of the above studies (and several more throughout the literature), we are building a picture of the properties of both the magnetospheric boundaries and of the upstream solar wind and magnetosheath regions. In order to complete this picture we wish to draw on the most complete set of data possible. To this end, in this paper we compile a comprehensive set of magnetopause and bow shock crossings for the entire Cassini mission from Saturn orbit insertion in 2004 to mission end in 2017, and use these crossings to enable study of boundary properties and of the regions (solar wind and magnetosheath) that they bracket. In section 2 we present the complete set of boundary crossings and explain the selection method. In section 3 we analyze the properties of the boundaries, drawing on magnetopause and bow shock models to infer upstream solar wind dynamic pressures and standoff distances for all crossings. In section 4 we discuss the results, and in section 5 we present a brief summary.

2. Data Set and Crossing List

The first stage of this work involved the painstaking task of searching by eye through the entire Cassini magnetometer (MAG) data set from just prior to Saturn Orbit Insertion in 2004 until the final orbits in late 2017 (Dougherty et al., 2004). We examined all apoapse intervals and regions where the spacecraft was close to expected nominal boundary locations in particularly fine detail (1-s resolution data over time scales of 2–3 hr) to search for the characteristic signatures of magnetopause and bow shock crossings, and labeled crossing times to the nearest minute. For magnetometer data, we used the Kronocentric Solar Magnetospheric (KSM) Saturn-centered system, where the positive x axis points toward the Sun, positive z axis points north such that the x - z plane contains Saturn's magnetic dipole axis, and the positive y axis points toward dusk. Where available (prior to instrument switch-off in 2012), we cross-checked all candidate crossings against data from the Cassini Plasma Spectrometer (CAPS) instrument (Young et al., 2004). Examples of crossings are shown later in Figure 1. Crossings beyond mid-2012 have been compiled from magnetometer data alone.

As a starting point, we consulted two previously compiled boundary crossing lists: (i) a list of both magnetopause and bow shock crossings posted on the MAPSView webpage (<http://mapskp.cesr.fr/BSMP/index.php>) spanning the interval 2004 day 179 to 2007 day 349 and compiled via visual identification of MAG and CAPS data (H.J. McAndrews, S.J. Kanani, A. Masters, and J.C. Cutler) and (ii) a list of magnetopause crossings spanning 2004 to October 2010 and May 2012 to February 2013 (Pilkington et al., 2015a). We included the crossings from these catalogues into our final list, giving precedence to the selection from the first (MAPSView) catalogue for cases where both catalogues had crossings (presumed to represent the same boundary encounter) listed with time stamps offset by a few minutes. We also independently confirmed all of these crossings by eye with both magnetometer and plasma data, and in several cases added missed

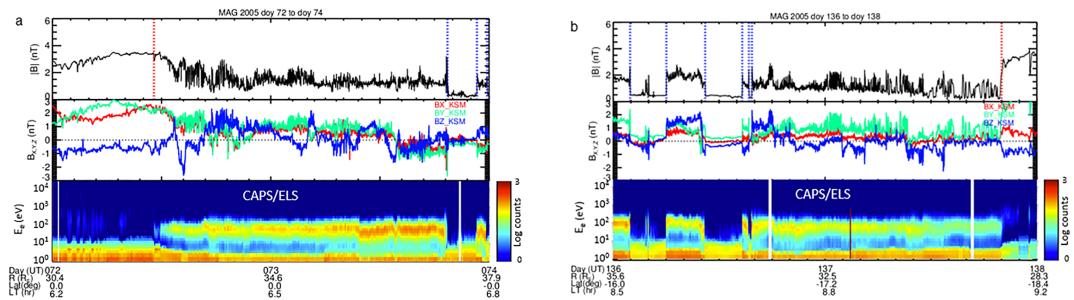


Figure 1. (a and b) Example magnetopause and bow shock crossings. The top panels show the total magnetic field strength, with bow shock crossings marked by vertical blue dotted lines, and magnetopause crossings marked by vertical red dotted lines. The middle panel in both figures shows the field components in the KSM coordinate system, colored as detailed in the figure legend. The bottom panels show electron spectrograms from CAPS/ELS with detector- and actuation-averaged counts (proportional to energy flux) plotted as a function of energy, with corresponding color bar to the right of the plot. Spacecraft ephemeris data are given at the bottom of the plots.

crossings or labeled data gaps. Aside from its complete coverage of the Cassini mission, one of the main advantages of our list is its self-consistency: there are no gaps or “errors” in the list, unlike previous catalogues. Specifically, there are no incomplete crossing progressions: that is, if an inbound bow shock crossing were then followed by a data gap, with the next interval of data showing an outbound magnetopause crossing, we know that the spacecraft must have crossed inbound over the magnetopause at least once during the data gap. We have employed a set of labels to account for such instances: in the table in the supporting information we note the *region* that the spacecraft was sampling at the time of the start of any data gap (e.g., S_SW, S_SH, or S_SP for intervals which start in the solar wind, magnetosheath, or magnetosphere, respectively). We do the same to note the region that the spacecraft was sampling at the end of any data gap (e.g., E_SW, E_SH, E_SP for intervals which end in the solar wind, magnetosheath, or magnetosphere, respectively). Thus, we deem our list to be ideal for region identification, with a wealth of future possibilities to use it to study the statistical properties of the solar wind, magnetosheath, or even the outer magnetosphere.

For the creation of the list itself, bow shock crossings are the easiest to identify: On one side the solar wind displays quiet, low-magnitude IMF and relatively cold ions and electrons ($<\sim 10$ eV, with the ions visible only very near the direction radial to the Sun), while on the other side the magnetosheath displays turbulent, enhanced IMF with characteristic field fluctuations (including mirror mode compressions) and heated ion and electron energy spectra (cf., Thomsen et al., 2018, for examples of characteristic particle spectra). For a spacecraft moving from solar wind into magnetosheath there is usually a clear increase in magnetic field strength, often accompanied by an “overshoot” feature (Russell et al., 1982). In rare cases where a bow shock crossing was unclear from the MAG data alone, inbound bow shock crossings could be identified from CAPS data by sharp increases in both the density and temperature of the plasma (and sharp decreases for outbound bow shock crossings).

Magnetopause crossings can be identified by both a change in the character and direction of the magnetic field. For inbound crossings, the field should change from the more turbulent fluctuations characteristic of the magnetosheath to the steadier field of the magnetosphere, accompanied by a rotation of the field to a southward (magnetospheric) orientation. For cases where the crossings are ambiguous from MAG data alone, CAPS data generally show a change from the steady electron energy spectra of the magnetosheath (higher density, lower temperature electrons) to the more variable magnetospheric populations (lower density, higher-temperature electrons; again, see Thomsen et al., 2018, for examples).

Boundary layers of intermediate field and plasma properties can often be present adjacent to boundary crossings. These can form due to mixing of plasma populations (e.g., via reconnection or the Kelvin-Helmholtz instability; e.g., Masters et al., 2011). For the purposes of generating this list, we have erred on the side of characterizing boundary layers close to the magnetopause as “magnetosphere,” thus placing the boundary crossing at the outer edge of the boundary layer-type behavior. This means that intervals that are characterized as “magnetosheath” based on the crossing list tend to have the characteristics of “purer”

sheath, with fewer boundary layer contaminations. Readers with a specific interest in boundary layer physics are encouraged to use this list as a stepping-off point for closer examination of relevant intervals.

Figures 1a and 1b show examples of inbound and outbound magnetopause and bow shock crossings that display the characteristics outlined above. In Figure 1a, which covers the interval from day 72 to 74 of 2005, Cassini was outbound on the dawn flank, observing a clean magnetopause crossing on day 72 at 11:09 in both magnetic field and plasma data, followed by an extended interval in the magnetosheath, where noisy, turbulent magnetic field is evident along with higher-energy electrons. Cassini then crossed the bow shock into the solar wind at 19:25, followed by a pair of in-out bow shock crossings later that day. Figure 1b shows another set of crossings, this time from the interval 2005 days 136–138, when Cassini was inbound prenoon. The spacecraft observed several clean bow shock crossings on day 136 followed by an extended interval in the sheath, and then a clear inbound magnetopause crossing on day 137 at 20:00.

While we have endeavored to be as thorough as possible in the identification of crossings (examining 1-min resolution magnetometer data by eye over the entire mission), it is always possible that some small-scale, short-duration crossings have been missed, or that the timings of our crossings may not precisely match the timings that could be derived from other instruments. Such timing ambiguities are an almost unavoidable feature of a multiinstrument data set. The shortest time interval between successive crossings is 1 min (three pairs with this separation), but the vast majority of events are separated by 10 min or longer. As mentioned above, the identification has been made based primarily on Cassini magnetometer data with validation against CAPS where possible. We look for the clearest magnetic deflections (e.g., well-defined magnetic ramps, or overshoots in the case of bow shock crossings), and our uncertainty in the identification of the magnetic transition is of order several minutes at most. In terms of multiple crossings within relatively short intervals, we note that such crossings have often been spatially averaged in previous modeling studies to remove any bias due to boundary waves, rapid boundary motion, or spacecraft trajectories parallel to the expected boundary surface which might result in an increased number of crossings over a short interval. We do not conduct any such spatial averaging here, but include the list of all crossings that we identified. In our statistical analysis of these crossings, we do, however, normalize the occurrence of boundary crossings within a given bin by the number of opportunities Cassini had to find the boundary within that bin (see below for a more complete discussion). Readers wishing to focus on small-scale features or to pursue empirically based boundary modeling are encouraged to use the list as a starting point for closer inspection.

3. Results

3.1. Statistical Location of Boundaries

Figure 2 shows the trajectory of Cassini from 2004 to 2017 in dark grey, with the locations of magnetopause crossings (Figure 2a) and bow shock crossings (Figure 2b) marked as red and blue filled circles, respectively. The spacecraft orbits covered all local times and provided ample coverage of the dayside, with flank coverage deeper at dawn than at dusk. In total there are 2,118 magnetopause crossings and 1,243 bow shock crossings in our list. In Figure 2, models of the magnetopause (Kanani et al., 2010) and bow shock (Went et al., 2011) are employed to plot average curves for solar wind dynamic pressures of 0.01 and 0.1 nPa, which span the typical range of values seen upstream of Saturn (Jackman & Arridge, 2011), with crossings lying outside this range likely to be associated with intervals of slightly deeper rarefaction or stronger compression than is typical.

While Figure 2 gives a sense of the spread of crossings, Figure 3 shows histograms of range, local time, and latitude, for the full spacecraft trajectory and for the magnetopause and bow shock crossings over the interval from 2004 day 175 to 2016 day 250. This includes the Saturn Orbit Insertion (SOI) maneuver during which the first inbound bow shock and magnetopause crossings were observed (2004 days 179 and 180, respectively), through to the last recorded inbound bow shock and magnetopause crossings on days 201 and 242 of 2016, respectively (thereafter Cassini's orbit had an apoapsis too low to encounter the magnetopause or bow shock). The histograms of magnetopause and bow shock crossings (middle and right-hand columns) show the number of crossings within a given bin, normalized to Cassini's total dwell time in that bin (in days). These normalized distributions therefore correspond to the probability of observing a boundary crossing in each spatial bin.

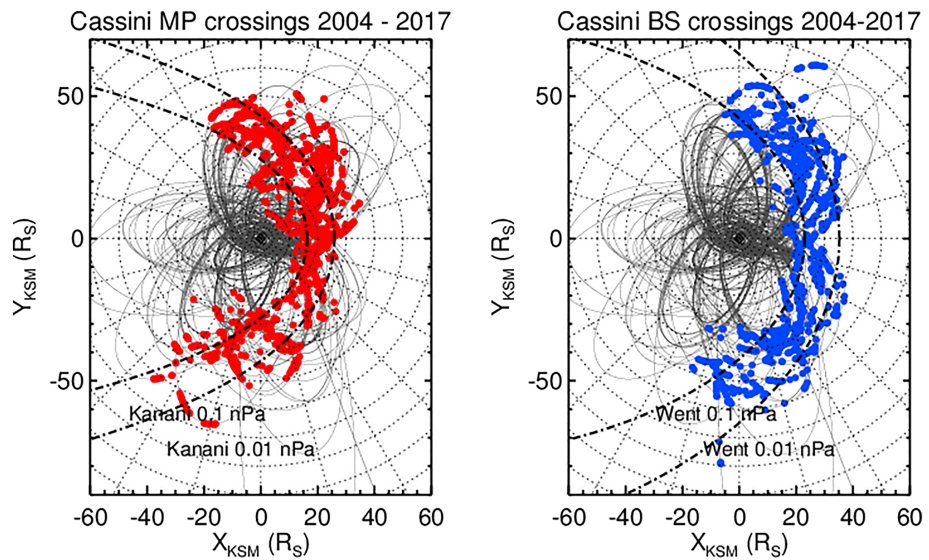


Figure 2. Location of magnetopause and bow shock crossings spanning the entire Cassini mission, overplotted on top of the trajectory of Cassini (thin dark grey lines) from Saturn Orbit Insertion in July 2004 to the start of 2017. (a) Magnetopause crossings as red dots. Model magnetopause locations based on Kanani et al. (2010) for solar wind dynamic pressures of 0.01 and 0.1 nPa are shown as thick black dot-dashed lines. (b) Bow shock crossings as blue dots. Model bow shock locations based on Went et al. (2011) for solar wind dynamic pressures of 0.01 and 0.1 nPa are shown as thick black dot-dashed lines.

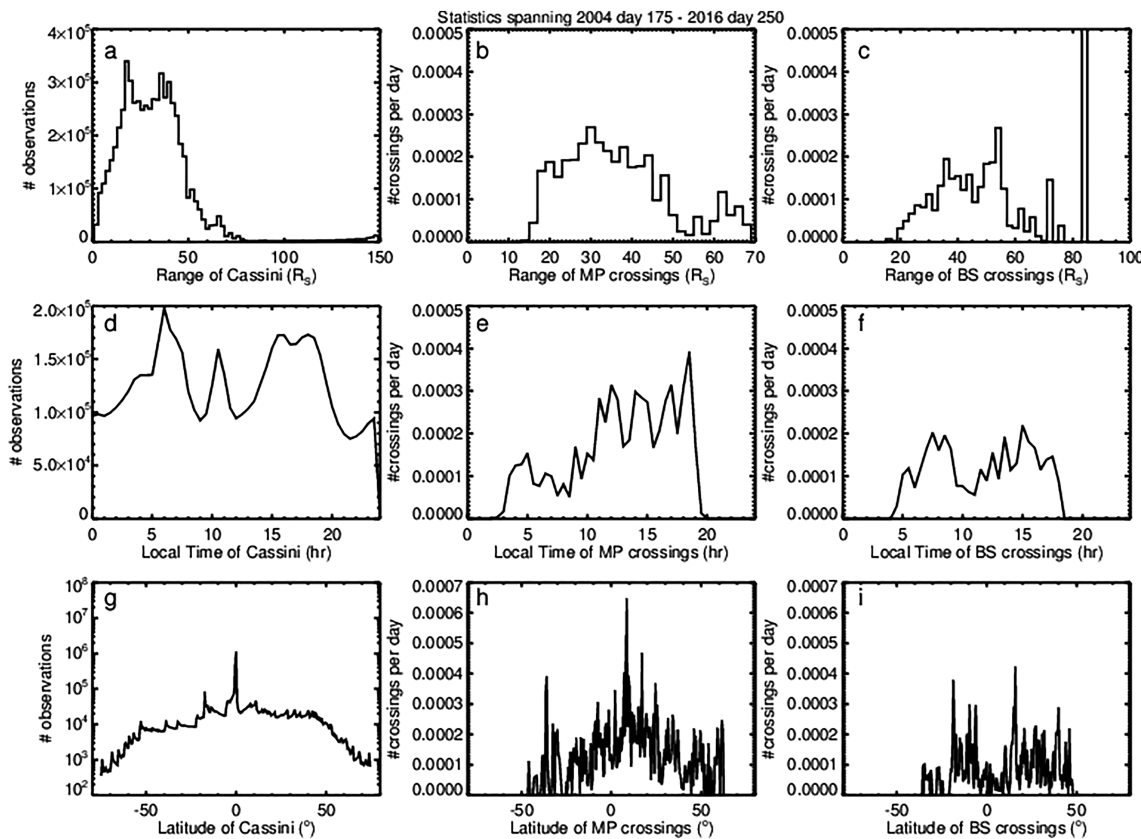


Figure 3. (a–c) Histograms of range in $2 R_S$ bins, (d–f) local time in 0.5-hr bins, and (g–i) latitude in 0.5° bins of the (left-hand column) spacecraft trajectory, (middle column) magnetopause crossings, and (right-hand column) bow shock crossings. The magnetopause and bow shock crossings are normalized to time spent in each location bin.

The top row of panels shows the radial distance spread. The approach maneuver prior to SOI involved an inbound trajectory from radial distances of $\sim 90 R_S$ on 2004 day 175 with one further capture orbit which took the spacecraft to $\sim 150 R_S$ later in 2004 before settling into the main series of revolutions which typically traversed radial distances out to $\sim 50 R_S$, with the exception of some deeper tail coverage (out to $68 R_S$) in 2006. Cassini encountered the magnetopause at radial distances ranging from 14.5 to $68.2 R_S$, with the normalized distribution of crossings peaking near $\sim 30 R_S$. It is important to note that these values represent the distance at which the spacecraft encountered the magnetopause (over the full range of local time and latitudes), and not the associated nose standoff distance. In later sections we will explore the use of models to track crossings to their nose standoff and examine patterns and links to upstream solar wind conditions therein. Bow shock crossings were observed at radial ranges of 17.3 to $85.1 R_S$, and the normalized distribution shows a peak at $\sim 55 R_S$.

The second row of panels in Figure 3 shows the distribution in local time. Magnetopause crossings span the range 2.8 to 20.8 hr, with the normalized distribution illustrating a preference for magnetopause crossings postnoon. Such an asymmetry may reflect a more dynamic magnetopause postnoon, or it may be an artifact of spatial coverage and long-term variations in the solar wind properties. For example, Thomsen et al. (2018) have noted that the prenoon magnetosheath intervals generally occurred during times when the solar wind speed was above average. The bow shock crossings do not display such a skew. Overall, bow shock crossings were spread across local times from 4.7 to 18.4 hr.

Finally, the bottom panels of Figure 3 show the spread of latitude, clearly illustrating that the spacecraft spent much of its time sampling near-equatorial latitudes (note the log y axis scale in Figure 3g). In fact, Cassini spent 50% of the interval shown at latitudes between -10° to $+10^\circ$. Once normalized to dwell time, the magnetopause crossings appear relatively evenly spread across latitude, with a moderate local peak at the highest positive latitudes, likely representing clusters of magnetopause crossings in the later stages of the mission. The bow shock crossing distribution shows a skew toward northerly latitudes.

3.2. Using Boundary Positions to Infer Upstream Solar Wind Conditions

The boundary-crossing list serves as a vehicle to infer the solar wind conditions upstream of Saturn at the time of the crossing. To this end we employ two models: Kanani et al. (2010) and Went et al. (2011), who modeled the magnetopause and bow shock surfaces, respectively. We briefly describe the model details here, but refer the interested reader to the original papers for more in-depth description of their properties.

3.2.1. Range of Applicability of Magnetopause and Bow Shock Models

The Kanani et al. (2010) magnetopause model was built from a catalogue of magnetopause crossings between June 2004 and January 2006, employing pressure balance between the solar wind dynamic pressure on the upstream side of the boundary and the measured magnetic and thermal pressures (assumed to be dominated by particles observed by the CHEMS instrument above 3 keV) on the magnetospheric side. In the model the distance R from the planet to a point on the magnetopause is described by

$$R = R_0 \left(\frac{2}{1 + \cos\theta} \right) \quad (1)$$

where θ is the angle between the x axis (KSM coordinates) and a vector from Saturn to the point on the magnetopause. R_0 is the nose stand-off distance of the magnetopause ($\theta = 0$) and is given by

$$R_0 = a_1 D_p^{-a_2} \quad (2)$$

where D_p is the upstream solar wind dynamic pressure. K specifies the flaring of the magnetopause and is given by

$$K = a_3 + a_4 D_p \quad (3)$$

where the model coefficients a_1 to a_4 are calculated from the fits to the model and have the values (10.3, 0.20, 0.73, 0.4), as listed in Table 1 in the Kanani et al. (2010) paper. For each of our magnetopause crossings, we know R and θ and wish to determine the associated value of D_p . However, the above equations are not easily rearranged to do this calculation of D_p directly. We thus instead calculate θ for each crossing as $\cos^{-1}(X_{\text{KSM}}/R)$,

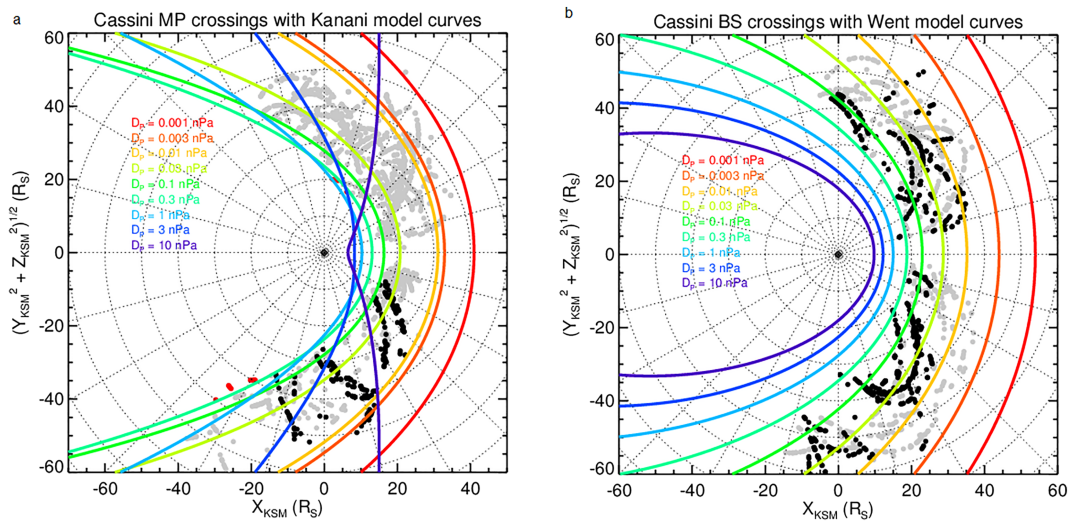


Figure 4. (a) Magnetopause surfaces based on the Kanani et al. (2010) model, for dynamic pressure values from 0.001 to 10 nPa with colors corresponding to the legend on the figure. Black dots ($n = 260$) represent magnetopause crossings during the interval upon which the Kanani model was built (note that the Kanani paper itself used a list of 191 crossings (McAndrews, 2007) over that interval, spatially averaged to 68 crossings). Grey dots ($n = 1,855$) represent magnetopause crossings from our list post-January 2006. Red dots ($n = 13$) represent crossings where the inferred D_P was >0.3 nPa, where we suggest that the model should not be applied. (b) Bow shock surfaces based on the Went et al. (2011) model, for dynamic pressure values of 0.001 to 10 nPa with colors corresponding to the legend on the figure. Black dots ($n = 581$) represent bow shock crossings during the interval upon which the model was built, with grey dots ($n = 662$) representing crossings outside of this time interval.

and then create a large (2,000-element) array with possible values of dynamic pressure, evenly logarithmically spaced between values of 0.001 and 10 nPa. These values have been chosen because they span the full range of measured dynamic pressures upstream of Saturn (Jackman & Arridge, 2011). For each magnetopause crossing on the list, we find the value of D_P that produces a model R at the known θ that equals the real R at which the crossing was observed. We thus assign the associated dynamic pressure to that crossing.

There may be some caveats to matching the full set of Cassini magnetopause crossings to inferred dynamic pressures using the Kanani formalism: (i) the Kanani model is based on just two years of measurements and thus does not cover all solar cycle or seasonal conditions. (ii) The crossings which were used to construct the model are more limited in local time (and latitude) than the crossing list that we have produced from the full mission. The impact of this may be that flank observations, particularly those in the deeper tail, may not be as well fitted by the model because the full impact of flaring may not be accounted for. And (iii) the model formalism can give double-valued solutions at large D_P and θ .

In order to explore these possible limitations, in Figure 4a we plot the Kanani model curves for a range of dynamic pressure values from 0.001 to 10 nPa. As mentioned above, the Kanani model was built using crossings observed between June 2004 and January 2006, and these are shown as black dots, while crossings thereafter are shown as lighter grey dots. On examination of the model curves, it is evident that above $D_P = 0.3$ nPa, the behavior of the solutions becomes counterintuitive, with the flaring increasing with increasing D_P and creating double-valued D_P solutions for a given R , especially at larger θ . Based on this, we have decided to place a limit on the applicability of the Kanani model (for the purpose of inferring upstream D_P or nose standoff distance from our crossings). We place this limit at $D_P > 0.3$ nPa. There are 13 such crossings in our list. Nine of these 13 crossings are on the dawn flank with $\theta > 110^\circ$, while a further four are toward dusk, at radial distances between 17 and 21 R_S . We have colored these 13 excluded points red in Figure 4a, leaving 2,105 crossings from our list where the Kanani model can be applied to infer upstream conditions.

The Went et al. (2011) semiempirical bow shock model was constructed using observations made during the flybys of Pioneer 11, Voyager 1, and Voyager 2, along with data from Cassini covering 2004 to 2010. Their

model describes the average shape of the bow shock surface and considers how this boundary moves with changing solar wind dynamic pressure. The key equation that relates the position of a crossing to the dynamic pressure is

$$R = (1 + \varepsilon) c_1 D_P^{\frac{c_1}{1+\varepsilon \cos \theta}} \quad (4)$$

where, in line with equation (1) above, R is the distance from the planet to a point on the boundary (in this case the bow shock) and θ is the angle between the x axis (KSM coordinates) and the vector from Saturn to that point on the bow shock. Parameters ε , c_1 , and c_2 are coefficients given in Table 1 of the Went et al. (2011) paper and have the values (0.84, 15, 5.4). Equation (4) can be solved analytically for D_P , and thus, our method to retrieve an associated solar wind dynamic pressure for each observed bow shock crossing is simply to put the observed values of R and θ for each of the crossings in our list into a rearranged equation (4) and directly retrieve D_P . Similar caveats apply here as for the Kanani magnetopause model: relying on a model constructed from a set of crossings that only span a subset of the full Cassini mission may mean that certain seasonal or solar cycle conditions and certain regions of local time or latitude are not as well sampled as others, and thus, the boundary position may not be so well constrained by the model in certain regions. In order to test these possible limitations, in Figure 4b we examine the Went model curves for a range of dynamic pressure values from 0.001 to 10 nPa. The Went model used several crossings from the Pioneer and Voyager era, which we have not included here, but the primary empirical database for their model was Cassini bow shock crossings up until July 2010, which we show as black dots. Crossings from our list post-July 2010 are shown as grey dots. Unlike in Figure 4a, where the behavior of the Kanani model becomes counterintuitive at large D_P and large θ , the Went bow shock curves make physical sense at increasing D_P , and we see the expected/intuitive relationship where flaring decreases with pressure, yielding a very streamlined bow shock surface on the nightside for the highest pressures. The crossings that were used to build the model are relatively symmetric in local time and span a fairly wide range of D_P values, so our confidence in using the Went model to infer upstream D_P and nose standoff distance for our full range of crossings is high.

3.2.2. Application of Magnetopause and Bow Shock Models to Infer Upstream Conditions

Magnetopause and bow shock models can represent very powerful tools to enable us to infer the upstream solar wind dynamic pressure and the associated expected magnetopause or bow shock standoff distance at any time when Cassini intercepted the boundaries. In Figure 5 we explore the range of upstream dynamic pressure and magnetopause standoff distance that correspond to the observed magnetopause crossings. In Figure 6 we do the same for the bow shock crossings.

Figure 5a shows the value of D_P that would have been required (using equations (1)–(3)) to produce a magnetopause crossing at each point in the Cassini orbit over the entire mission, for all $D_P < 0.3$ nPa. Figure 5b shows the occurrence distribution for this full set of “observable” dynamic pressures. This panel therefore represents the “dwell time” of Cassini for each D_P bin. Figure 5c shows the inferred D_P for each actual magnetopause encounter, and the black curve in Figure 5d shows the resulting D_P occurrence distribution. Finally, the red curve in Figure 5d is the D_P distribution for the actual crossings, normalized by the Cassini dwell time in each D_P bin.

Figures 5a and 5b indicate that according to the Kanani model, the Cassini trajectory provided access to upstream dynamic pressure values between 0.001 and 0.3, with a sharp peak at ~0.1 nPa. In Figures 5c and 5d, the D_P inferred from the actual magnetopause boundary crossings (i.e., the 2,118 – 13 = 2,105 magnetopause crossings from our list) varies over nearly the full range accessible to Cassini.

The occurrence distribution normalized to dwell time (red curve, Figure 5h) shows standoff distances ranging from ~15 to ~38 R_S , peaking broadly between ~18 and 25 R_S . There is little evidence in Figure 5h for a double-peaked distribution inferred by previous authors from a more limited data set (e.g., Achilleos et al., 2008).

More recently, Pilkington et al. (2015a) employed seven years of Cassini data to examine the behavior of the magnetopause boundary. They compared their distribution of the inferred standoff distance to several possible model fits (including normal, lognormal, bimodal). They found a bimodal distribution to be the most likely to describe the underlying population, but noted that it does not capture the behavior of the magnetopause entirely. The distribution Figure 5h, which is the most complete empirical distribution possible (given

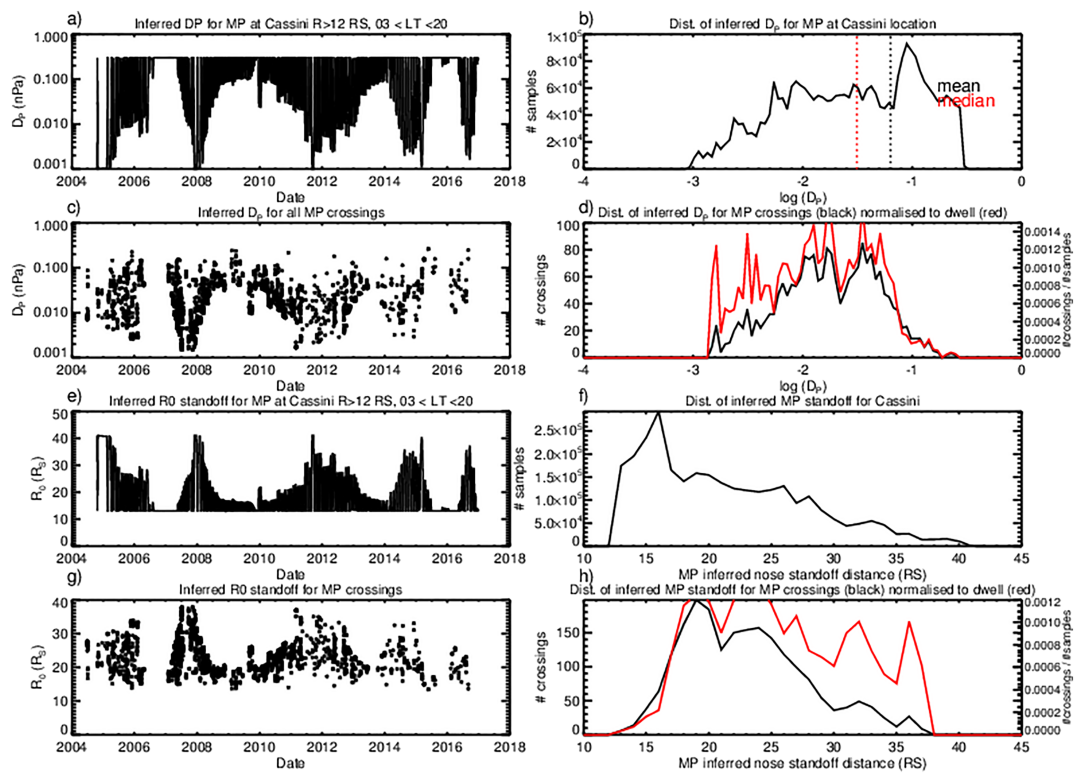


Figure 5. Timelines and distributions of solar wind dynamic pressure (D_P) and magnetopause nose standoff distance (R_0) inferred using the Kanani et al. (2010) magnetopause model. (a and b) The timeline and distribution of D_P that would be inferred for a magnetopause crossing at each point along the Cassini trajectory where $R > 12 R_S$ and $03 < LT < 20$ hr, while any values of $D_P > 0.3$ nPa are discarded. Vertical dotted black and red lines in (b) show the mean and median of the distribution, respectively. (c and d) The timeline and distribution of D_P inferred for magnetopause crossings from the list (with similar applicability criteria on D_P and θ). In (d) the black curve shows the distribution of D_P for magnetopause crossings, with the red curve normalized to dwell time (i.e., divided by the distribution from the Cassini trajectory in (b)). (e-h) Similar progression for the inferred magnetopause nose standoff distance.

that it is based on the entire Cassini data set), shows strong similarities to Pilkington et al.'s distribution, with an even more prominent shoulder at higher standoff distances (up to $38 R_S$).

Figure 6 shows the same parameters as Figure 5 and in the same format, but in this case applied to the bow shock. Here we have applied the Went et al. (2011) bow shock model to the full Cassini data set, and to the list of bow shock crossings in order to infer the upstream solar wind dynamic pressure and the associated expected bow shock standoff distance. Unlike the Kanani model, the Went model formalism does not require any limits to be placed on the applicability of the inferred D_P or the initial θ location of the spacecraft.

The possible inferred D_P from the Cassini trajectory spreads to higher values for the bow shock than for the magnetopause but this is purely a feature of the 0.3-nPa cutoff applied to the magnetopause distributions shown in Figure 5. When we examine the inferred D_P for the set of bow shock crossings in the second row (Figures 5c and 5d), we find that most encounters with the bow shock lead to inferred upstream dynamic pressures between 0.01 and 0.1 nPa. The third (Figures 5e and 5f) and fourth (Figures 5g and 5h) rows of Figure 6 show the inferred standoff distance values. The distribution of inferred standoff distances in Figure 5h, based on 1,243 crossings and normalized to Cassini dwell time (red curve), ranges from ~ 18 to $50 R_S$, with most values between 20 and $40 R_S$.

3.2.3. Comparison of Inferred Solar Wind Conditions With MHD Model Prediction

The magnetopause and bow shock crossings considered here span the entire Cassini mission (and thus a range of solar cycle and seasonal conditions). It is instructive to examine how the distribution of solar wind dynamic pressures inferred from linking these crossing times to boundary models compares to the distribution of solar wind dynamic pressure predicted by solar wind models such as the Michigan Solar

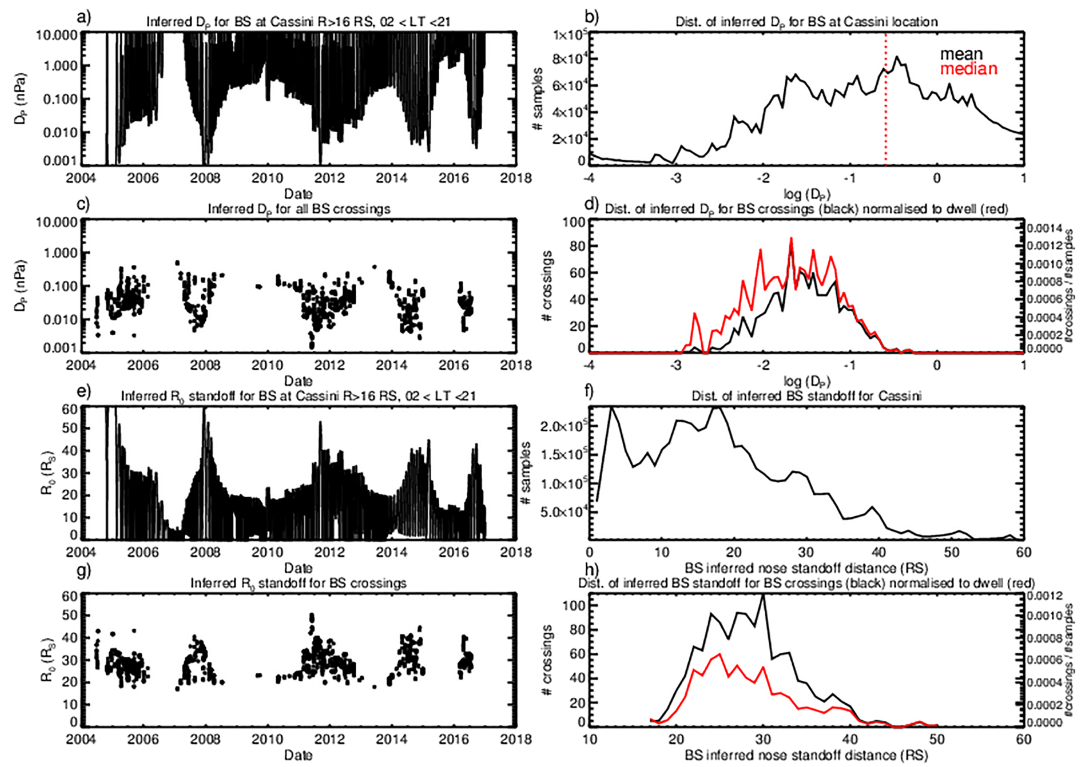


Figure 6. Timelines and distributions of solar wind dynamic pressure (D_P) and magnetopause nose standoff distance (R_0) inferred using the Went et al. (2011) bow shock model. Figure in the same format as Figure 5.

Wind Model (mSWiM; Zieger & Hansen, 2008). This comparison is shown in Figure 7, where the inferred D_P values from the magnetopause and bow shock crossings, normalized to spacecraft dwell times, are compared with the mSWiM-derived values of D_P for the same time range as the observations. The distributions of inferred D_P for magnetopause and bow shock crossings are largely similar (albeit with a slightly higher proportion of bow shock crossings seen at higher inferred dynamic pressures). It is important to note that the dynamic pressures used by Kanani and Went in their modeling work were themselves indirect: for example, Went used 32-hr averages of the solar wind velocity taken from mSWiM, and this averaging would produce some inaccuracies during times when V_{SW} was changing rapidly. Furthermore, Zieger and Hansen (2008) found that significant offsets in shock arrival time were not uncommon, and thus, reliance on these values for further modeling can introduce some inaccuracies. It is likely that these effects are a contributor to the slight offset between the magnetopause and bow shock D_P distributions. This offset in turn could make a small quantitative impact on the analysis of rapid crossings, but overall we expect the findings to be qualitatively robust. The distribution from the mSWiM model is offset roughly a factor of 2 lower than the inferred distributions from boundary crossings. The median and mean values (in nPa) for the three distributions are (bow shock: ~0.03 median, 0.05 mean; magnetopause: ~0.02 median, 0.03 mean; and mSWiM: 0.01 median, 0.02 mean).

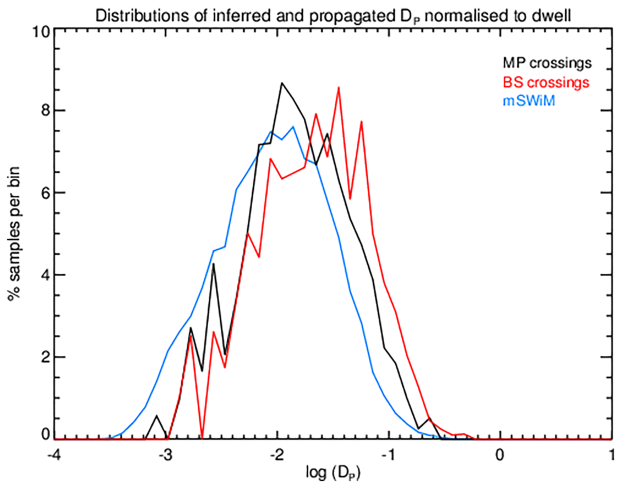


Figure 7. Distributions of solar wind dynamic pressure D_P inferred from magnetopause crossings with the Kanani et al. (2010) model (black trace) and inferred from bow shock crossings with the Went et al. (2011) model (red trace), compared with values at Saturn produced by the mSWiM propagated solar wind model between 2004 and end of 2016 (blue trace). All distributions have 50 bins over the range of $\log(D_P)$ shown, and the y axis is normalized to the total number of samples. Both the bow shock and magnetopause distributions are normalized to spacecraft dwell time.

The offset relative to the mSWiM D_P distribution may be due in part to the limitations of spacecraft trajectory. In order to see a boundary in a particular range of D_P , Cassini must spend time in the region in which the boundary would reside. The nature of Cassini apoapses was such that the

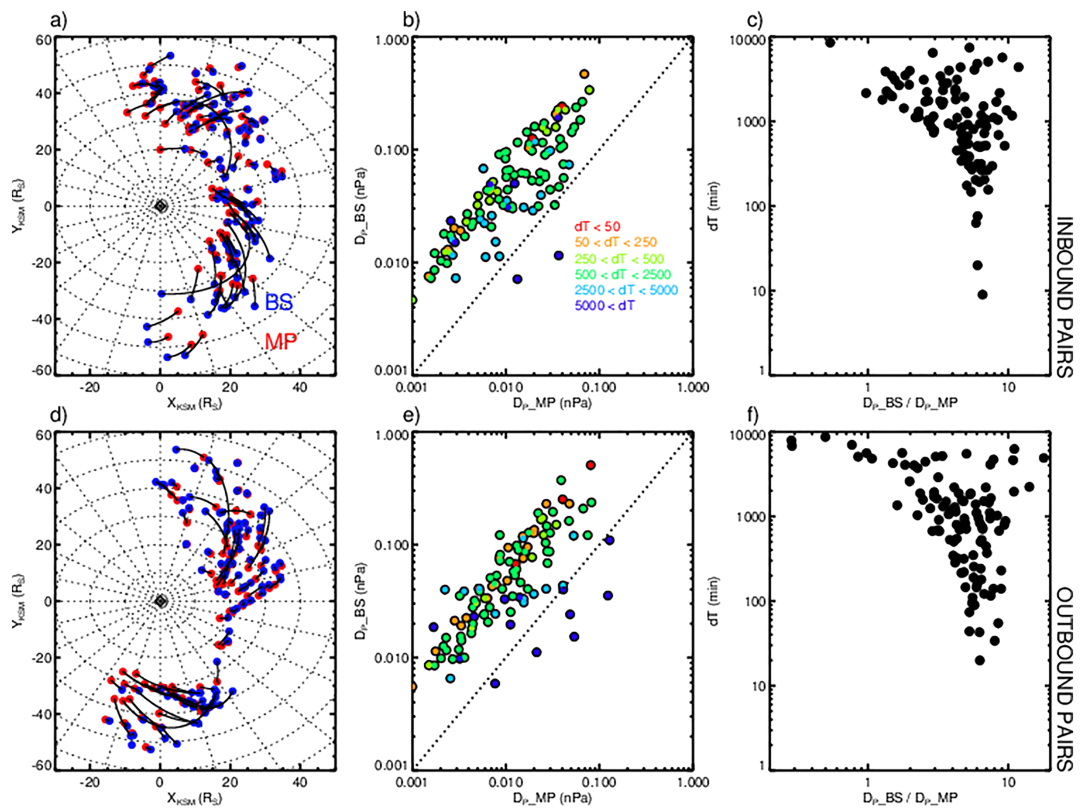


Figure 8. (a) Locations of 109 inbound traversals of Saturn's magnetosheath, identified by sequential inbound crossings (“pairs”) of the bow shock then magnetopause. (b) The inferred solar wind dynamic pressure from the Kanani (magnetopause) and Went (bow shock) models for the pairs of inbound crossings. This is color coded according to the time difference in minutes (dT) between crossings. (c) The ratio of inferred D_P for bow shock to inferred D_P for magnetopause versus dT between crossings. (d–f) Data from 109 outbound magnetosheath traversals, bounded by sequential outbound crossings of the magnetopause and bow shock, respectively. These panels are in the same format as (a)–(c).

spacecraft had relatively few opportunities to encounter boundaries where they would be if $D_P < 0.001$ nPa (cf., Figures 5a and 6a) and indeed saw none (Figure 4). By contrast, Cassini spent a great deal of time on numerous orbits within the region where the magnetopause would be found if 0.001 nPa $< D_P < 0.01$ nPa, and quite a few were observed in this range. There is thus a bias against low D_P introduced by the range of the Cassini trajectory, and this bias is even more severe for the bow shock crossings, which require coverage at even larger radial range than for the magnetopause at the same D_P . On the other hand, trajectory limitations do not explain the larger percentage of inferred D_P values at the high end ($D_P > 3 \times 10^{-2}$ nPa) compared to mSWiM. Thus, the offset seen in Figure 7 may be real and not yet fully explained. More detailed exploration of the distribution of D_P values from mSWiM should certainly be the focus of future work (albeit outside of the scope of this paper). Avenues for exploration could include comparison with alternative solar wind propagation models, and examination of mSWiM predictions in other locations (such as at Jupiter, compared with in situ Juno data).

3.3. Rapid Traversals of the Magnetosheath

The list of boundary crossings that we present in this work has a multitude of possible uses, but the final aspect that we focus on here is exploring direct traversals of the magnetosheath, where an inbound bow shock crossing is followed by an inbound magnetopause crossing, or vice versa where an outbound magnetopause crossing is followed by an outbound bow shock crossing. There are 109 such inbound pairs and 109 outbound pairs in our data set. Figure 8 shows the summary of the properties of pairs of magnetopause and bow shock crossings. The left-hand panels (Figures 8a and 8d) show the path of the spacecraft between successive boundary crossings for inbound (Figure 8a) and outbound (Figure 8d), such that the black traces correspond to the time spent by the spacecraft in the magnetosheath. Bow shock crossings are marked with blue

dots, and magnetopause crossings with red dots. For stationary boundaries “inbound” pairs, where an inbound bow shock crossing is followed by an inbound magnetopause crossing, should occur during portions of the spacecraft trajectory where Cassini was inbound toward the planet, and vice versa for “outbound” pairs. Indeed, most (82/109) of the inbound pairs (BS→MP) occur during the inbound portions of the spacecraft trajectory, and most (91/109) of the outbound pairs (MP→BS) occur during the outbound portions of the trajectory. For such crossings, the blue dots lie at greater radial distances than the red ones. Examples of these more typical cases of “direct traversals” are shown above in Figures 1a and 1b. In Figure 1a, Cassini spent ~32 hr in the magnetosheath between consecutive outbound magnetopause and bow shock crossings at radial distances of ~32.4 and ~37.3 R_S , respectively. In Figure 1b, Cassini spent ~29 hr in the magnetosheath between consecutive inbound bow shock and magnetopause crossings at radial distances of 33.7 and 29.1 R_S , respectively. There are, however, a number of crossings in the list and displayed in Figure 8 where the bow shock crossing (blue) occurred very close to or even inward of the corresponding magnetopause crossing (red). Such crossings are of particular interest as indicators of dynamic boundary behavior. In the data set shown in Figure 8, there are 14 and 25 inbound and outbound pairs, respectively, with time separations less than 300 min.

The middle panels (Figures 8b and 8e) show the inferred solar wind dynamic pressure for each pair of crossings (inbound Figure 8b, outbound Figure 8e), with the color code corresponding to the time between crossings, as given in minutes by the legend. In both inbound and outbound cases Figure 8 shows that the inferred dynamic pressure is higher for the bow shock than the magnetopause crossing of a given pair, particularly for rapid crossings (<500 min). This is clearly seen in the right-hand panels (Figures 8c and 8f) where the ratio between the inferred dynamic pressure, D_P , for bow shock and magnetopause is shown as a function of sheath crossing duration. For rapid inbound crossings, a sequence of higher D_P at the bow shock than at the magnetopause is consistent with the spacecraft, initially in the solar wind, crossing the bow shock, and subsequently the magnetopause under conditions of decreasing D_P ; that is, the boundaries expand outward. Similarly, for rapid outbound magnetosheath crossings, the spacecraft is initially in the magnetosphere and crosses the magnetopause and then the bow shock under conditions of increasing D_P ; that is, the boundaries move inward. In both cases, the dynamic pressure at the bow shock crossing exceeds that at the magnetopause crossing. Thus, in general, the pressure relationship shown in Figures 8b and 8c and 8e and 8f shows that rapid inbound crossings are linked to expansions of the magnetosphere, and rapid outbound crossings are linked to compressions of the magnetosphere. Further, most of the direct magnetosheath crossings, especially for relatively short crossing times <100 min, appear to occur during fairly substantial changes in the dynamic pressure (factors of ~6–7 and higher).

3.3.1. Estimating Boundary Velocities

The rapid inbound or outbound crossing pairs offer the opportunity to roughly estimate the speed of the boundaries in response to sudden variations in the dynamic pressure. Figure 9 illustrates the approach. For an inbound magnetosheath crossing (Figure 9a), a decreasing dynamic pressure results in first a bow shock crossing at time t_1 , then subsequently a magnetopause crossing at time t_2 . We estimate the dynamic pressure at t_1 from the observed bow shock crossing location using the Went et al. (2011) bow shock model (equation (4)):

$$D_{p,1} = D_{p,Went}(t_1)$$

For this dynamic pressure, the Went model predicts a bow shock nose standoff distance of (equation (4) with $\theta = 0$):

$$R_{0,BS}(t_1) = c_1 D_{p1}^{\frac{-1}{2}} \quad (5)$$

Using the Kanani et al. (2010) model, the magnetopause nose standoff distance for the dynamic pressure D_{p1} is (equation (2))

$$R_{0,MP}(t_1) = a_1 D_{p1}^{-a_2} \quad (6)$$

Similarly, at the subsequent crossing of the magnetopause at t_2 , the Kanani model provides the value of D_{p2} as described above in section 3.2.1:

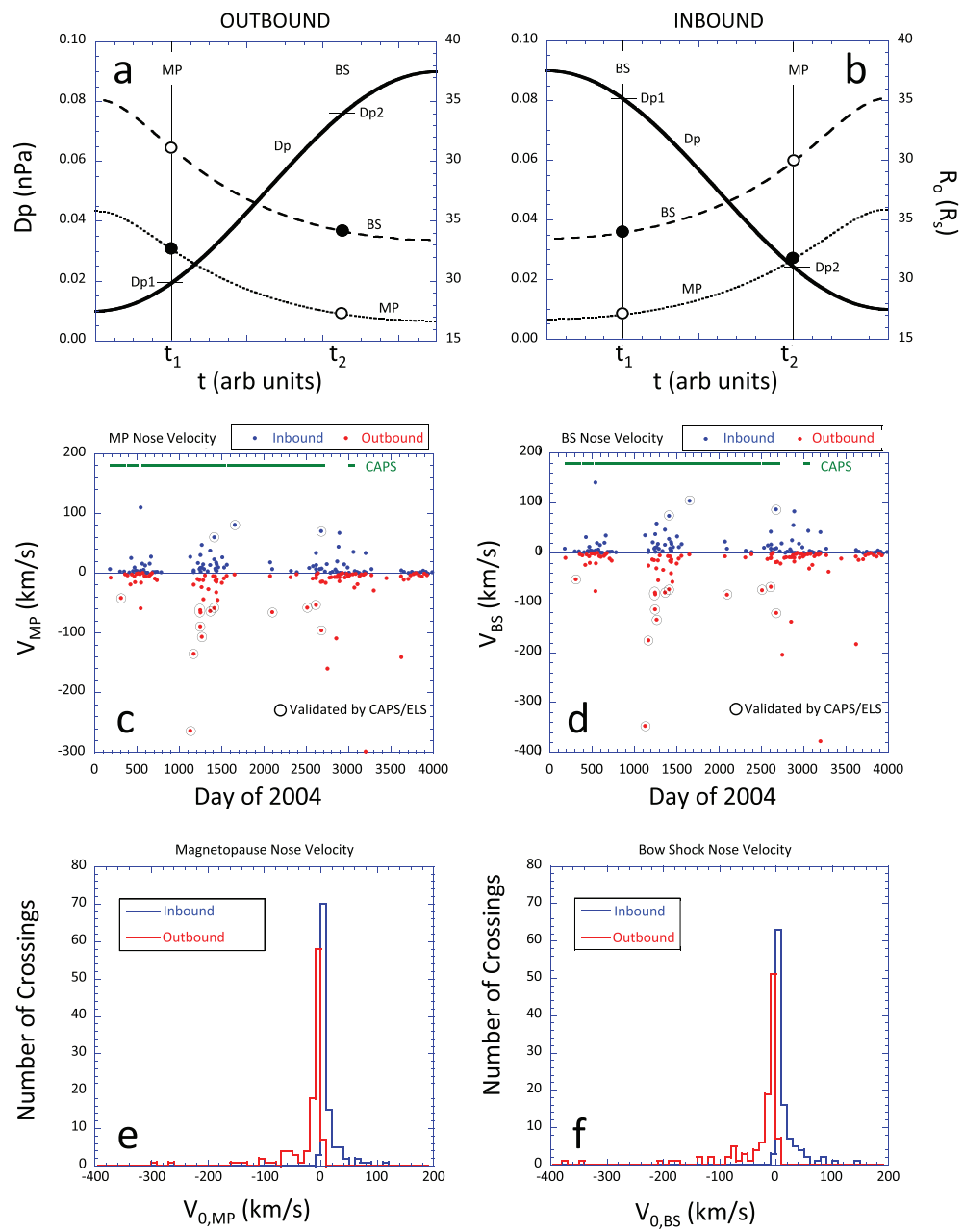


Figure 9. Illustration of boundary locations during (a) increasing D_p (outbound boundary pair) and (b) decreasing D_p (inbound boundary pair). Derived nose velocities for (c) magnetopause and (d) bow shock for all the crossing pairs, plotted as a function of time in days from 1 January 2004. Inbound crossings are indicated by blue symbols, and outbound crossings by red symbols. Point circled with black have been specially validated with CAPS data. Occurrence histograms of inferred boundary nose velocities for (e) magnetopause and (f) bow shock. Blue curves correspond to inbound crossings, and red ones to outbound crossings.

$$D_{p2} = D_{pKanami}(t_2),$$

which then yields the standoff distance for the magnetopause

$$R_{0,MP}(t_2) = a_1 D_{p2}^{-a_2} \quad (7)$$

and for the bow shock

$$R_{0,BS}(t_2) = c_1 D_P^{\frac{1}{c_2}} \quad (8)$$

Finally, the boundary speeds at the nose are estimated as

$$V_{0,MP} \approx \frac{R_{0,MP}(t_2) - R_{0,MP}(t_1)}{t_2 - t_1} \quad (9)$$

and

$$V_{0,BS} \approx \frac{R_{0,BS}(t_2) - R_{0,BS}(t_1)}{t_2 - t_1} \quad (10)$$

A similar procedure can be followed for outbound crossings (Figure 9b).

Figures 9c and 9d show the resulting magnetopause and bow shock nose velocities for the set of inbound and outbound crossing pairs, and Figures 9e and 9f show the corresponding occurrence histograms. Figure 9 presents velocities derived for both the magnetopause and bow shock for each crossing pair, but these two velocities are not actually independent. Rather, the ratio of $V_{0,BS}/V_{0,MP}$ is $\sim 1.27 \pm 0.02$ for all the crossings, both inbound and outbound. That is due to the fact that the formalism we have adopted is that the Kanani and Went models apply at every instant in time. From equations (5) and (6), the ratio of bow shock to magnetopause nose distances under this assumption is

$$\frac{R_{0,BS}}{R_{0,MP}} = \frac{c_1}{a_1} D_P^{(a_2 - 1/c_2)} = 1.46 D_P^{0.015} \quad (11)$$

For a typical $D_P = 0.01$ nPa, the ratio would be 1.36. The dependence on D_P is weak, so the bow shock and magnetopause nose distances maintain a roughly constant ratio as D_P varies. Thus, if the magnetopause nose distance varies by a factor of x during a crossing, the bow shock distance must also vary by a factor $\sim x$ during the same time, so the bow shock speed will be ~ 1.36 times the corresponding magnetopause speed. The fact that the ratio of the derived velocities is ~ 1.27 instead of 1.36 is due to the small influence of the changing D_P during the transition and that the D_P for the bow shock crossing is consistently greater than that for the magnetopause crossing, as discussed above (cf., Figure 8).

As expected, Figure 9 shows that the vast majority of inbound crossings (104/109) correspond to times when the nose velocity was positive (outward expansion), whereas the vast majority of outbound crossings (101/109) correspond to negative velocities (inward compression). For almost all of the crossings shown in Figure 9, the estimated velocities are small, < 20 km/s. Of the 10 crossings with “counterintuitive” nose velocities (inbound crossing with negative V, outbound crossing with positive V), none has $|V| > 0.9$ km/s for either boundary, and all have $\Delta t > 2,160$ min. Thus, these crossings simply represent occasions when the time between magnetopause and bow shock crossings was so long that the conditions for the sequential boundary crossings were largely unrelated.

There are a few noteworthy outliers in Figure 9, where the sense of expansion or compression of the magnetosphere matches with the direction of the associated boundary crossings, and with nose speeds reaching several tens of kilometers per second and higher. As can be seen by the derivation above, these correspond to very short crossing times ($t_2 - t_1$). We have looked with particular interest at these very rapid crossings; in Figures 9c and 9d the circled points are those that we have carefully re-confirmed with CAPS data. The confirmed events produce estimated magnetopause nose speeds as high as 80 km/s for inbound crossings and 263 km/s for outbound crossings.

3.3.2. Rapid Traversals Case Studies

To illustrate the utility of the set of boundary-pair crossings identified from the full set of crossings, Figures 10 and 11 present observational details of two specific events. Figure 10 shows a complete inbound magnetosheath crossing that occurred on 29 April 2011 (day 119), over the span of ~ 2.5 hr. Figure 10a is a color spectrogram of the electron count rate observed by CAPS/ELS, similar to those shown in Figure 1. Figure 10b shows the 1-D electron density and temperature derived from the ELS data (Lewis et al., 2008). Within the solar wind (labeled SW) derived values are invalid and therefore omitted from the figure. Figures 10c–10f show the total magnetic field and its components in KRTP coordinates. The

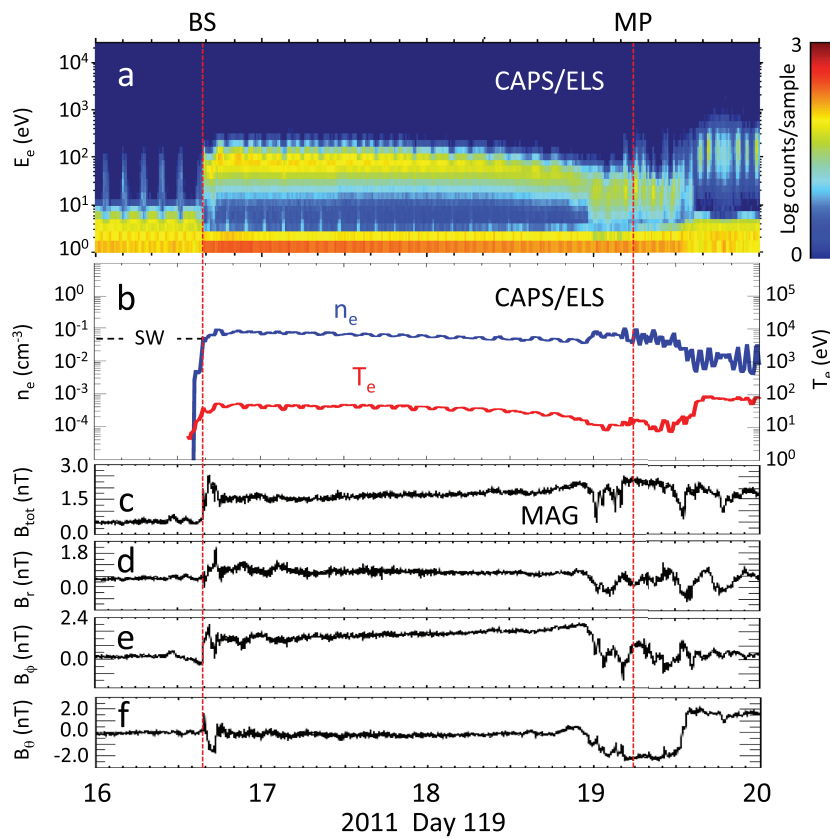


Figure 10. Plasma and magnetic field data for a rapid inbound crossing of the magnetosheath on 29 April 2011 (day 119). (a) Energy-time spectrogram of electron count rate, proportional to the energy flux, measured by the CAPS ELS. (b) Electron density and temperature derived from ELS data. (c–f) Magnetic field magnitude and KRTP components. The bow shock (BS) and magnetopause (MP) crossings are marked with vertical red dotted lines. Electron moments within the solar wind (sw) are invalid and therefore not plotted.

magnetopause and bow shock crossings are indicated with vertical red dashed lines. Use of the Kanani and Went models produced dynamic pressures of 0.00281 and 0.0202 nPa at the magnetopause and bow shock crossings, respectively, consistent with the above-noted association of inbound crossings with magnetospheric expansions due to decreasing D_P . This sevenfold decrease in pressure actually probably happened while the spacecraft was still in the solar wind, prior to the 1639 UT bow shock crossing, because there is little evidence for any significant density drop within the magnetosheath itself. Using the above analysis of the timing of the crossings, we find an outward magnetopause nose speed for this event of ~ 70 km/s.

Figure 11 has the same format as Figure 10 and shows data from the fastest magnetosheath crossing in the data set with CAPS validation, the outbound boundary crossings on 2 February 2007 (day 33). For this event the magnetopause and bow shock crossings were separated by only 20 min, which yielded an inward magnetopause nose speed of 263 km/s in the above analysis. Use of the Kanani and Went models produced dynamic pressures of 0.0807 and 0.507 nPa, at the magnetopause and bow shock crossings, respectively, consistent with the association of outbound crossings with magnetospheric compressions due to rising D_P . The dynamic pressure at the magnetopause crossing (0.0807 nPa) is already on the high end of the occurrence distribution (Figure 5d), and the inferred D_P at the bow shock is among the highest we have seen (Figure 6d).

In Figure 11 the electron spectral signatures of the magnetopause and bow shock are quite clear (cf., Figure 1), but in addition, there is an apparent change in the character of the plasma midway through the magnetosheath crossing (at $\sim 2,345$), which shows the arrival of a much denser, colder solar wind plasma. While a full analysis of this interval is beyond the scope of the present study, it is worth noting that the mSWIM

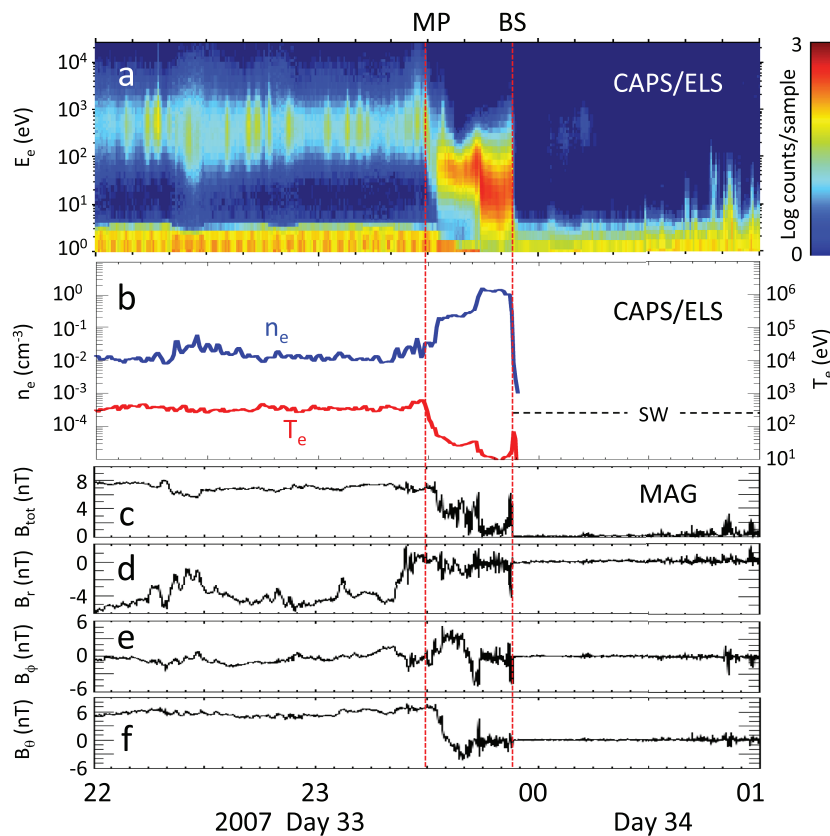


Figure 11. Same format as Figure 10, for a very rapid outbound crossing of the magnetosheath on 2 February 2007 (day 33). This 20-min interval between magnetopause and bow shock is the shortest in the boundary crossing data set described in this paper and corresponds to an inferred inward magnetopause nose velocity of 263 km/s.

model predicts an increasing dynamic pressure during this time interval, with a decreasing temperature. However, the time scale for the predicted changes is on the order of days, so one interesting outcome of this event may be that structure in the solar wind maintains a substantially sharper variation than predicted by MHD models.

4. Discussion

We have presented a comprehensive list of magnetopause and bow shock crossings made by the Cassini spacecraft at Saturn over the course of its 13-year mission. The list consists of 2,118 magnetopause crossings and 1,243 bow shock crossings, identified primarily by their distinctive signatures in 1-min magnetometer data, but validated as much as possible with electron data from CAPS. The uncertainty in the identified crossings times is at most several minutes. The list contains no incomplete crossing progressions; data gaps are identified as to the region (solar wind, magnetosheath, magnetosphere) in which the spacecraft was at the start and stop of the gap. Thus, the list should be very valuable for studies of region identification. The spatial coverage of the Cassini mission was excellent, both in radial distance and local time, and this new list contains crossings throughout the dayside and well onto both flanks.

Published models of the magnetopause (Kanani et al., 2010) and the bow shock (Went et al., 2011) have been used to infer the upstream dynamic pressure and nose standoff location corresponding to each of the crossings in the new list. We have reported that the Kanani et al. formalism produces an unrealistic shape and double-valued solutions at large dynamic pressure D_P and nose angle θ . Therefore, in the statistics of the inferred dynamic pressure and nose distances, magnetopause crossings with inferred $D_P > 0.3$ nPa have been discarded. This restriction only results in the exclusion of 13 crossings, however, so it is unlikely to affect our overall results. It is possible that a different model (e.g., Pilkington et al., 2015a) would not be susceptible to

these problems, which appear to derive from the D_P dependence of the flaring parameter used by Kanani et al. As noted by Pilkington et al., “it was found that the dynamic pressure has only a very small effect on the magnetospheric flaring, so can be safely neglected in future studies with minimal loss of model accuracy.” The Went bow shock model does not exhibit any such difficulties.

Our use of the Kanani et al. (2010) magnetopause model neglects the polar flattening and dawn-dusk asymmetries that have been documented by Pilkington et al. (2014, 2015b), as well as the important contribution of the internal magnetospheric plasma in helping to hold off the solar wind dynamic pressure (Pilkington et al., 2015a). Indeed, if we had used the Pilkington et al. (2015a) model, the inferred quantity would have been $D_P/(1 + \beta)$, rather than D_P alone, where β is the beta of the magnetospheric plasma just inside the magnetopause. Application of these more sophisticated models to the new database would be a worthwhile study for the future. We also note that the Alfvén Mach number would be expected to have a significant influence on the shape and structure of the bow shock. However, given that we do not have the required density or velocity measurements available for most of our crossings, we have neglected to consider the dependence on Alfvén Mach number (and note the Went and Kanani models similarly excluded examination of this parameter).

For the magnetopause, the occurrence distribution normalized to dwell time (red curve, Figure 5h) shows inferred standoff distances ranging from ~ 15 to $\sim 38 R_S$, peaking broadly between ~ 18 and $25 R_S$. There is also a prominent shoulder at higher standoff distances, up to $38 R_S$, but otherwise, little evidence for a double-peaked distribution inferred by previous authors (e.g., Achilleos et al., 2008).

For the bow shock, the distribution of inferred standoff distances, normalized to Cassini dwell time (Figure 6h), ranges from ~ 18 to $50 R_S$, with most values between 20 and $40 R_S$.

The occurrence distributions of D_P inferred from the magnetopause and bow shock crossings are quite similar to each other (Figure 7) but both appear to be about a factor of 2 higher than the dynamic pressures predicted at Saturn over this time interval by the mSWIM MHD model (Zieger & Hansen, 2008). The distribution derived from bow shock crossings shows slightly more events with higher D_P and slightly fewer with lower D_P than the distribution derived from magnetopause crossings. This difference may be partly attributable to the relative lack of opportunities to find the boundaries at large radial distances (low D_P), especially the bow shock.

In this data set, there are 218 instances of direct crossings of the magnetosheath, either an inbound bow shock crossing followed by an inbound magnetopause crossing or an outbound magnetopause crossing followed by an outbound bow shock crossing. Most of the former occur during an inbound part of the trajectory, whereas most of the latter occur during outbound portions. For these crossing pairs, the dynamic pressure inferred from the bow shock crossing always exceeds that inferred from the magnetopause crossing, as expected if outbound crossings arise from magnetospheric compressions and inbound crossings arise from magnetospheric expansions.

Using the Kanani and Went models for the magnetopause and bow shock locations, we have used the times of the two boundary crossings in these pairs to estimate the velocity of the magnetopause and bow shock nose. This calculation is based on the assumption that the Kanani and Went models apply instantaneously at each point in time. As pointed out based on recent MHD simulations of bow shock motion (Mejnertsen et al., 2018), this approximation is not likely to be strictly accurate since significant solar wind variations occur on time scales short compared to the transit time of a phase front over the shock surface. And as they further note, any observational analysis of shock speed is probably biased toward higher velocities because the spacecraft generally only encounters the shock when the shock is in motion. Nonetheless, within this simplifying assumption, we have estimated the shock and magnetopause velocities for the set of direct magnetosheath crossings.

Most of the direct crossings produce relatively low nose velocities (< 10 km/s), but there are some crossings that are quite short in time and lead to fast nose speeds, up to 263 km/s for the magnetopause and 346 km/s for the bow shock. Multispacecraft measurements of shock motion at the Earth have found shock speeds (not nose speeds, which are likely somewhat lower) that average near zero, with a standard deviation of 42 km/s, but with a significant number of examples where the speed exceeded 100 km/s (e.g., Meziane et al., 2014). Based on the work of Völk and Auer (1974), Meziane et al. interpreted their findings as indicating that at

the lower shock speeds, shock motion probably occurs primarily due to random fluctuations in solar wind parameters, whereas speeds above 100 km/s are probably due to solar wind discontinuities (for example, tangential discontinuities and interplanetary shocks). They found that dynamic pressure variations were the dominant factor producing fast shock motions. With no upstream solar wind monitor, it is difficult to test this conclusion for Saturn's bow shock, but the inferred dynamic pressures at the boundary crossings (Figure 8) certainly suggest that significant changes (both increases and decreases) of the dynamic pressure are associated with these events, especially when the magnetosheath crossing times are short.

Two individual examples of relatively brief complete magnetosheath crossings, one inbound and one outbound, have been presented. Both suggest relatively rapid variations in solar wind dynamic pressure ($<\sim$ hours) by factors of \sim 7. The second event, a very rapid outbound crossing shows clear evidence of a significant change in the plasma density while the spacecraft was crossing the magnetosheath, with the high-density region markedly cooler than the plasma it follows, showing that sharp increases in dynamic pressure over short periods do happen.

5. Summary

A new, comprehensive list of magnetopause and bow shock crossings made by the Cassini spacecraft at Saturn over the course of its 13-year mission has been introduced. The list consists of 2,118 magnetopause crossings and 1,243 bow shock crossings. Combination of these identified crossings with magnetopause and bow shock models produces occurrence statistics of solar wind dynamic pressure and of the nose standoff distances for both boundaries. The models also enable the estimation of nose standoff velocities for cases of direct traversals of the magnetosheath, both inbound and outbound. These velocities are typically <10 km/s but on occasion can be as much as 200–300 km/s. This nearly complete data set should enable numerous future studies of Saturn's interface with the solar wind.

Acknowledgments

The full list of magnetopause and bow shock crossings is provided as supporting information in the online version of this article and is available directly through the following

repository: 10.6084/m9.

figshare.9762323. We encourage those wishing to use the crossings times to contact C.M. Jackman directly with any queries about the most appropriate use of the information contained in the list. C.M.J. is supported by STFC fellowship ST/L004399/1. C.M.J. acknowledges work by Southampton students Harvey Brown and Luke Tunstall toward the crossing list. Part of this work emerged from collaborative discussions that took place during a visit of M.F.T. to the University of Southampton as a Diamond Jubilee Fellow. The support provided by the Diamond Jubilee Fellowship is gratefully acknowledged. Work at PSI was supported by the NASA Cassini program through JPL contract 1243218 with Southwest Research Institute. Calibrated data from the Cassini mission are available from the NASA Planetary Data System at the Jet Propulsion Laboratory (<https://pds.jpl.nasa.gov/>). We thank K. C. Hansen and B. Zieger for providing the solar wind properties from their mSWIM model (Zieger & Hansen, 2008). We acknowledge the use of the list of Cassini magnetopause and bow shock crossings compiled by H.J. McAndrews, S.J. Kanani, A. Masters, and J.C. Cutler (<http://mapskp.cesr.fr/BSMP/index.php>), as well as the list of magnetopause crossings compiled by N. Pilkington (Pilkington et al., 2015a) as a basis for the list presented here.

References

- Achilleos, N., Arridge, C. S., Bertucci, C., Jackman, C. M., Dougherty, M. K., Khurana, K. K., & Russell, C. T. (2008). Large-scale dynamics of Saturn's magnetopause: Observations by Cassini. *Journal of Geophysical Research*, 113, A11209. <https://doi.org/10.1029/2008JA013265>
- Burkholder, B., Delamere, P. A., Ma, X., Thomsen, M. F., Wilson, R. J., & Bagenal, F. (2017). Local time asymmetry of Saturn's magnetosheath flows. *Geophysical Research Letters*, 44, 5877–5883. <https://doi.org/10.1002/2017GL073031>
- Clarke, K. E., André, N., Andrews, D. J., Coates, A. J., Cowley, S. W. H., Dougherty, M. K., et al. (2006). Cassini observations of planetary-period oscillations of Saturn's magnetopause. *Geophysical Research Letters*, 33, L23104. <https://doi.org/10.1029/2006GL027821>
- Clarke, K. E., Andrews, D. J., Coates, A. J., Cowley, S. W. H., & Masters, A. (2010). Magnetospheric period oscillations of Saturn's bow shock. *Journal of Geophysical Research*, 115, A05202. <https://doi.org/10.1029/2009JA015164>
- Dougherty, M. K., Kellock, S., Southwood, D. J., Balogh, A., Smith, E. J., Tsurutani, B. T., et al. (2004). The Cassini magnetic field investigation. *Space Science Reviews*, 114(1–4), 331–383. <https://doi.org/10.1007/s11214-004-1432-2>
- Jackman, C. M., Achilleos, N., Bunce, E. J., Cowley, S. W. H., Dougherty, M. K., Jones, G. H., et al. (2004). Interplanetary magnetic field at ~ 9 AU during the declining phase of the solar cycle and its implications for Saturn's magnetospheric dynamics. *Journal of Geophysical Research*, 109, A11203. <https://doi.org/10.1029/2004JA010614>
- Jackman, C. M., & Arridge, C. S. (2011). Solar Cycle Effects on the Dynamics of Jupiter's and Saturn's Magnetospheres. *Solar Physics*, 274, 481–502. <https://doi.org/10.1007/s11207-011-9748-z>
- Jia, X., Hansen, K. C., Gombosi, T. I., Kivelson, M. G., Tóth, G., DeZeeuw, D. L., & Ridley, A. J. (2012). Magnetospheric configuration and dynamics of Saturn's magnetosphere: A global MHD simulation. *Journal of Geophysical Research*, 117, A05225. <https://doi.org/10.1029/2012JA017575>
- Kanani, S. J., Arridge, C. S., Jones, G. H., Fazakerley, A. N., McAndrews, H. J., Sergis, N., et al. (2010). A new form of Saturn's magnetopause using a dynamic pressure balance model, based on *in situ*, multi-instrument Cassini measurements. *Journal of Geophysical Research*, 115, A06207. <https://doi.org/10.1029/2009JA014262>
- Lewis, G. R., André, N., Arridge, C. S., Coates, A. J., Gilbert, L. K., Linder, D. R., & Rymer, A. M. (2008). Derivation of density and temperature from the Cassini-Huygens CAPS electron spectrometer. *Planetary and Space Science*, 56(7), 901–912. <https://doi.org/10.1016/j.pss.2007.12.017>
- Masters, A., Mitchell, D. G., Coates, A. J., & Dougherty, M. K. (2011). Saturn's low-latitude boundary layer: 1. Properties and variability. *Journal of Geophysical Research*, 116, A06210. <https://doi.org/10.1029/2010JA016421>
- McAndrews, H. J. (2007). PhD thesis, University of London.
- Mejnertsen, L., Eastwood, J. P., Hietala, H., Schwartz, S. J., & Chittenden, J. P. (2018). Global MHD simulations of the Earth's bow shock shape and motion under variable solar wind conditions. *Journal of Geophysical Research: Space Physics*, 123, 259–271. <https://doi.org/10.1002/2017JA024690>
- Meziane, K., Alrefay, T. Y., & Hamza, A. M. (2014). On the shape and motion of the Earth's bow shock. *Planetary and Space Science*, 93–94, 1. <https://doi.org/10.1016/j.pss.2014.01.006>
- Mistry, R., Dougherty, M. K., Masters, A., Sulaiman, A. H., & Allen, E. J. (2014). Separating drivers of Saturnian magnetopause motion. *Journal of Geophysical Research: Space Physics*, 119, 1514–1522. <https://doi.org/10.1002/2013JA019489>
- Pilkington, N. M., Achilleos, N., Arridge, C. S., Guio, P., Masters, A., Ray, L. C., et al. (2015a). Internally driven large-scale changes in the size of Saturn's magnetosphere. *Journal of Geophysical Research: Space Physics*, 120, 7289–7306. <https://doi.org/10.1002/2015JA021290>

- Pilkington, N. M., Achilleos, N., Arridge, C. S., Guio, P., Masters, A., Ray, L. C., et al. (2015b). Asymmetries observed in Saturn's magnetopause geometry. *Geophysical Research Letters*, 42, 6890–6898. <https://doi.org/10.1002/2015GL065477>
- Pilkington, N. M., Achilleos, N., Arridge, C. S., Masters, A., Sergis, N., Coates, A. J., & Dougherty, M. K. (2014). Polar confinement of Saturn's magnetosphere revealed by in situ Cassini observations. *Journal of Geophysical Research: Space Physics*, 119, 2858–2875. <https://doi.org/10.1002/2014JA019774>
- Russell, C. T., Hoppe, M. M., & Livesey, W. A. (1982). Overshoots in planetary bow shocks. *Nature*, 296(5852), 45–48.
- Sergis, N., Jackman, C. M., Masters, A., Krimigis, S. M., Thomsen, M. F., Hamilton, D. C., et al. (2013). Particle and magnetic field properties of the Saturnian magnetosheath: Presence and upstream escape of hot magnetospheric plasma. *Journal of Geophysical Research: Space Physics*, 118, 1620–1634. <https://doi.org/10.1002/jgra.50164>
- Sulaiman, A. H., Jia, X., Achilleos, N., Sergis, N., Gurnett, D. A., & Kurth, W. S. (2017). Large-scale solar wind flow around Saturn's non-axisymmetric magnetosphere. *Journal of Geophysical Research: Space Physics*, 122, 9198–9206. <https://doi.org/10.1002/2017JA024595>
- Thomsen, M. F., Coates, A. J., Jackman, C. M., Sergis, N., Jia, X., & Hansen, K. C. (2018). Survey of magnetosheath plasma properties at Saturn and inference of upstream flow conditions. *Journal of Geophysical Research: Space Physics*, 123, 2034–2053. <https://doi.org/10.1002/2018JA025214>
- Völk, H. J., & Auer, R. D. (1974). Motions of the bow shock induced by interplanetary disturbances. *Journal of Geophysical Research*, 79, 40–48.
- Went, D. R., Hospodarsky, G. B., Masters, A., Hansen, K. C., & Dougherty, M. K. (2011). A new semiempirical model of Saturn's bow shock based on propagated solar wind parameters. *Journal of Geophysical Research*, 116, A07202. <https://doi.org/10.1029/2010JA016349>
- Young, D. T., Berthelier, J. J., Blanc, M., Burch, J. L., Coates, A. J., Goldstein, R., et al. (2004). Cassini plasma spectrometer investigation. *Space Science Reviews*, 114(1-4), 1–112. <https://doi.org/10.1007/s11214-004-1406-4>
- Zieger, B., & Hansen, K. C. (2008). Statistical validation of a solar wind propagation model from 1 to 10 AU. *Journal of Geophysical Research*, 113, A08107. <https://doi.org/10.1029/2008JA013046>
- Zieger, B., Hansen, K. C., Gombosi, T. I., & De Zeeuw, D. L. (2010). Periodic plasma escape from the mass-loaded Kronian magnetosphere. *Journal of Geophysical Research*, 115, A08208. <https://doi.org/10.1029/2009JA014951>